

## Structural Dynamics of Two-Dimensional Ruddlesden-Popper Perovskites A Computational Study

Fridriksson, Magnus B.; Maheshwari, Sudeep; Grozema, Ferdinand C.

**DOI**

[10.1021/acs.jpcc.0c05225](https://doi.org/10.1021/acs.jpcc.0c05225)

**Publication date**

2020

**Document Version**

Final published version

**Published in**

Journal of Physical Chemistry C

**Citation (APA)**

Fridriksson, M. B., Maheshwari, S., & Grozema, F. C. (2020). Structural Dynamics of Two-Dimensional Ruddlesden-Popper Perovskites: A Computational Study. *Journal of Physical Chemistry C*, 124(40), 22096-22104. <https://doi.org/10.1021/acs.jpcc.0c05225>

**Important note**

To cite this publication, please use the final published version (if applicable).  
Please check the document version above.

**Copyright**

Other than for strictly personal use, it is not permitted to download, forward or distribute the text or part of it, without the consent of the author(s) and/or copyright holder(s), unless the work is under an open content license such as Creative Commons.

**Takedown policy**

Please contact us and provide details if you believe this document breaches copyrights.  
We will remove access to the work immediately and investigate your claim.

# Structural Dynamics of Two-Dimensional Ruddlesden–Popper Perovskites: A Computational Study

Published as part of *The Journal of Physical Chemistry virtual special issue “Josef Michl Festschrift”*.

Magnus B. Fridriksson, Sudeep Maheshwari, and Ferdinand C. Grozema\*

Cite This: *J. Phys. Chem. C* 2020, 124, 22096–22104

Read Online

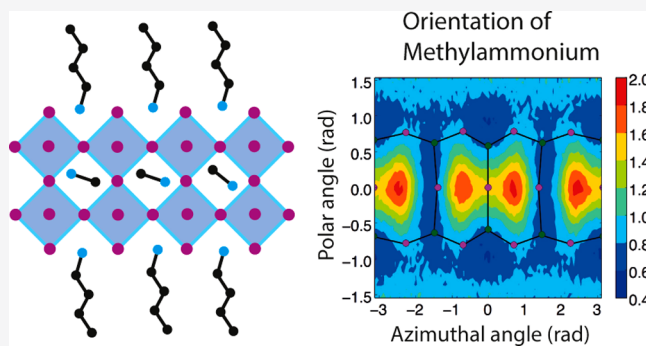
ACCESS |

Metrics & More

Article Recommendations

Supporting Information

**ABSTRACT:** Recently two-dimensional (2D) hybrid organic–inorganic perovskites have attracted a lot of interest as more stable analogues of their three-dimensional counterparts for optoelectronic applications. However, a thorough understanding of the effect that this reduced dimensionality has on dynamical and structural behavior of individual parts of the perovskite is currently lacking. We have used molecular dynamics simulations to investigate the structure and dynamics of 2D Ruddlesden–Popper perovskite with the general formula  $BA_2MA_{n-1}Pb_nI_{3n+1}$ , where BA is butylammonium, MA is methylammonium, and  $n$  is the number of lead–iodide layers. We discuss the dynamic behavior of both the inorganic and the organic part and compare between the different 2D structures. We show that the rigidity of the inorganic layer markedly increases with the number of lead–iodide layers and that low-temperature structural phase changes accompanied by tilting of the octahedra occurs in some but not all structures. Furthermore, the dynamic behavior of the MA ion is significantly affected by the number of inorganic layers, involving changes both in the reorientation times and in the occurrence of specific preferred orientations.



## INTRODUCTION

Over the past few years hybrid halide perovskite materials have attracted a lot of interest due to their impressive properties as photovoltaic materials.<sup>1–3</sup> This has led to high-efficiency solar cells, reaching efficiencies over 25%,<sup>4</sup> but applications in light-emitting diodes (LEDs),<sup>5–7</sup> photodetectors,<sup>8,9</sup> lasers,<sup>6,10</sup> and radiation detectors<sup>11–13</sup> are also rapidly emerging. Perovskites are characterized by a general  $ABX_3$  structure where A is a monovalent cation, often organic (methylammonium, formamidinium, cesium), B is a divalent cation (lead, tin), and X is a monovalent halide anion (iodide, bromide). The most studied perovskite for photovoltaic applications is  $(CH_3NH_3)PbI_3$  or methylammonium lead–iodide (MAPbI). In this material the A cation is the organic cation methylammonium (MA).

One of the major drawbacks of perovskites is that they are very sensitive towards air and moisture, causing a rapid degradation of devices when they are not properly encapsulated.<sup>14,15</sup> A possible approach to counter this is replacing (part of) the MA by a large organic cation, leading to a two-dimensional (2D) structure.<sup>16–21</sup> The large organic cation breaks up the structure in 2D layers of inorganic Pb–I octahedra separated by the large organic cations. The hydrophobic nature of the organic component protects the material from air and moisture, resulting in a higher

stability.<sup>17,18,22,23</sup> The most common 2D perovskites are Ruddlesden–Popper type materials that have a general  $(R-NH_3)_2A_{n-1}B_nX_{3n+1}$  structural formula.<sup>16,21</sup> In these structures, A, B, and X are the same as in the case of the 3D perovskite, but  $R-NH_3^+$  is a large monovalent ammonium cation that does not fit inside the 3D perovskite structure and hence is responsible for breaking up the structure into layers. Because the large cation does not have to fit into the inorganic metal–halide cage structure, there is considerable freedom in size and nature. The most common choices at present are the commercially available phenylethylammonium (PEA)<sup>24,25</sup> or aliphatics like *n*-butylammonium (BA),<sup>16,18,21</sup> but there are also examples of the incorporation of large conjugated molecules.<sup>26–30</sup> By modifying the ratio between the large  $(R-NH_3)$  and the small (A) organic cation, it is possible to systematically vary the number of inorganic perovskite layers ( $n$ ) between each spacer layer of the large organic cations. This

Received: June 9, 2020

Revised: September 10, 2020

Published: September 15, 2020



tuning of the layer thickness is accompanied by changes in the optoelectronic properties.<sup>21</sup> When  $n = 1$ , no small A cation is present, and a single layer of Pb–I octahedra is sandwiched between the large organic cations. For larger values of  $n$ , the number of inorganic perovskite layers in between the organic layers increases, but at the same time small organic cations are introduced in the materials. These changes have a large effect on the local environment of the individual molecules in the system. The optoelectronic properties (exciton diffusion, fluorescence quantum yield) are intricately linked to the (dynamic) structural properties of the 2D layers in the material.<sup>31</sup> As shown recently, structural variations in the layer of large organic cations or altering the number of inorganic layer can result in significant changes in the exciton diffusion properties,<sup>32,33</sup> which is believed to be a result of differences in the rigidity of the 2D structure. Therefore, it is of considerable interest to explore the structural dynamics of 2D perovskites and how it depends on the number of inorganic layers.

In this work we have performed model potential molecular dynamics (MD) simulations on 2D Ruddlesden–Popper perovskites with varying number of inorganic layers ( $n = 1–4$ ) as well as on the corresponding 3D perovskite. In all cases lead and iodide form the inorganic layer and where appropriate the large cation is BA and the small cation is MA. We have studied the effect of the number of layers on the individual parts of the structure: the inorganic layer, the small organic cation, and the large organic cation. In this way we gain insight into the rigidity of the inorganic layer, the mutual angles of the octahedra, and the rotational diffusion of the small and large organic cations. These simulations indicate that the interplay between the dynamics of the inorganic lattice and the organic cations is very subtle and that the behavior of the different parts of the materials are strongly interconnected. The presence of the organic cations has a pronounced effect on the structure of the inorganic lattice, but the motion of the organic cations is also strongly correlated to distortions of the inorganic lattice. The results show that it is possible to tune the distortions in the inorganic lattice by changing the organic cations but increasing the layer thickness of the inorganic part generally makes the lattice more rigid. Both the average structure and rigidity of the inorganic lattice and the rotational dynamics of the organic cations will affect the electronic structure of the materials.<sup>34–36</sup>

## METHODS

All molecular dynamics simulations were performed by using the LAMMPS software.<sup>37</sup> We have adopted the force field from the work of Mattoni et al.<sup>38</sup> on 3D methylammonium lead–iodide. In this force field the interactions between Pb and I are described with a Buckingham potential, while the organic–organic interactions are described by Lennard–Jones terms which are derived from the standard Amber force field.<sup>39</sup> The inorganic–organic interactions are described by either a Lennard–Jones (when hydrogen is involved) or a Buckingham potential. To make the force field transferrable between the different materials that we consider, we deviate from the Mattoni force field in one respect: the partial charges for the Coulomb interactions. We assign the full formal charges +2 and –1 to the lead and iodide ions (versus +2.02 and –1.13 in the Mattoni force field). In addition, the organic cations have a full +1 charge that is distributed over all atoms as obtained from an electronic structure calculation. This leads to small deviations as can be seen if the results for 3D perovskite are

compared to our previous work which did not use full formal charges.<sup>40</sup> This leads to a decrease of the temperature at which the phase transition is observed (Figure S1). We have explicitly chosen to adapt the way charges are assigned to the individual ions because this leads to a straightforward transferrable force field that can be adapted easily to structures for different  $n$  and other organic cations. We recognize that this may affect the detailed description, for instance, of phase transitions; however, it does make it possible to make a direct qualitative comparison between different related structures. The latter would not be possible if the force field was optimized for each compound individually.

The partial charges on the individual atoms in MA and BA were obtained by fitting them to the electrostatic potential from a density functional theory calculation (B3LYP/cc-pVQZ) using the CHelpG approach<sup>41</sup> in the Gaussian09 software.<sup>42</sup>

The initial structures used for the 2D perovskites and the 3D perovskite were obtained from experimental crystal structures.<sup>21,43</sup> In the case of the 3D perovskite the simulations were performed on a supercell of  $10 \times 10 \times 10$  unit cells, while for the 2D perovskite a supercell of  $10 \times 10$  unit cells was used. The direction perpendicular to the lead–iodide layer was not replicated for the 2D systems, but it should be noted that the unit cell already contains two Pb–I layers. In all cases periodic boundary conditions were used in all directions, and the volume was kept constant.

For all simulations an initial temperature of 400 K is used where the system is allowed to equilibrate for 1 ns with a time step of 1 fs. This time step was used throughout all simulations discussed. After the equilibration, the temperature is lowered to the desired temperature with a fixed annealing rate of 125 K/ns. Once the desired temperature is reached, the system is again allowed to equilibrate for 1 ns before a 100 ps production run is performed. Throughout the production run the positions of all atoms are recorded.

## RESULTS AND DISCUSSION

To gain insight into the structural and dynamical properties of 2D Ruddlesden–Popper perovskites, we have performed a series of MD simulations as outlined above. Following these MD simulations, we now analyze the trajectories that were obtained to compare their structural features. More specifically, we want to understand what the effect will be on the rigidity of the lead–iodide layers and the orientation and motion of the MA and BA ions. We start by focusing on the lead–iodide layer and its rigidity, after which we discuss the dynamics of the organic component.

**Structure and Dynamics of the Pb–I Lattice.** To compare the rigidity of the lead–iodide layer between different structures, we compare the positions of the lead atoms throughout the simulations. For each simulation the coordinates of every lead atom at every time step is extracted, and a histogram of the out of layer coordinate (the  $z$ -coordinate) is made. Depending on the initial structure, the histograms will differ in number and positions of peaks. However, each peak will in all cases represent a single layer of lead ions in the structure. Every peak is fitted with a simple Gaussian function, and the standard deviation is extracted. The latter is an indicator of the structural flexibility of the lead atoms in each layer. In a more rigid layer, the movement of the lead atoms in the direction perpendicular to the layer will be diminished and therefore give rise a narrower peak with a

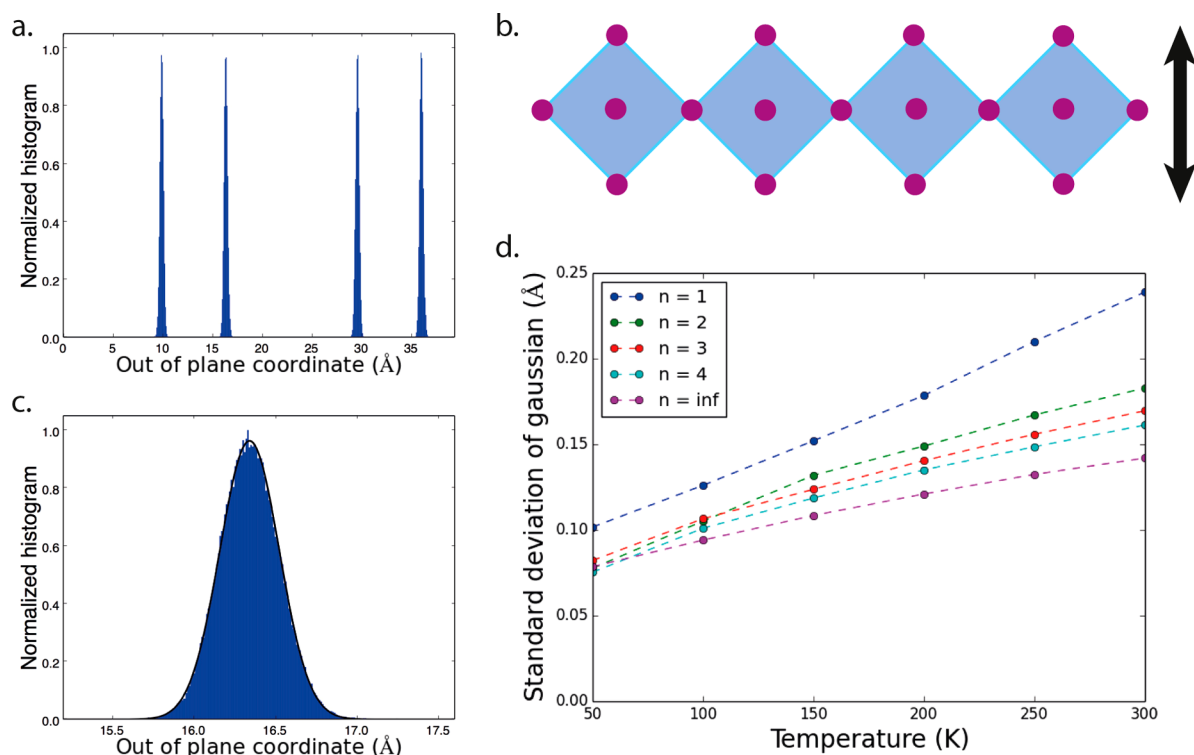


**Figure 1.** Motion of lead atoms. (a) Histogram of out of layer coordinates for an  $n = 2$  simulation. (b) Lead–iodide octahedral layer with the out of layer direction highlighted. (c) Single peak from the histogram at close with a fitted Gaussian. (d) Average standard deviation of the fitted Gaussian for each structure versus temperature.

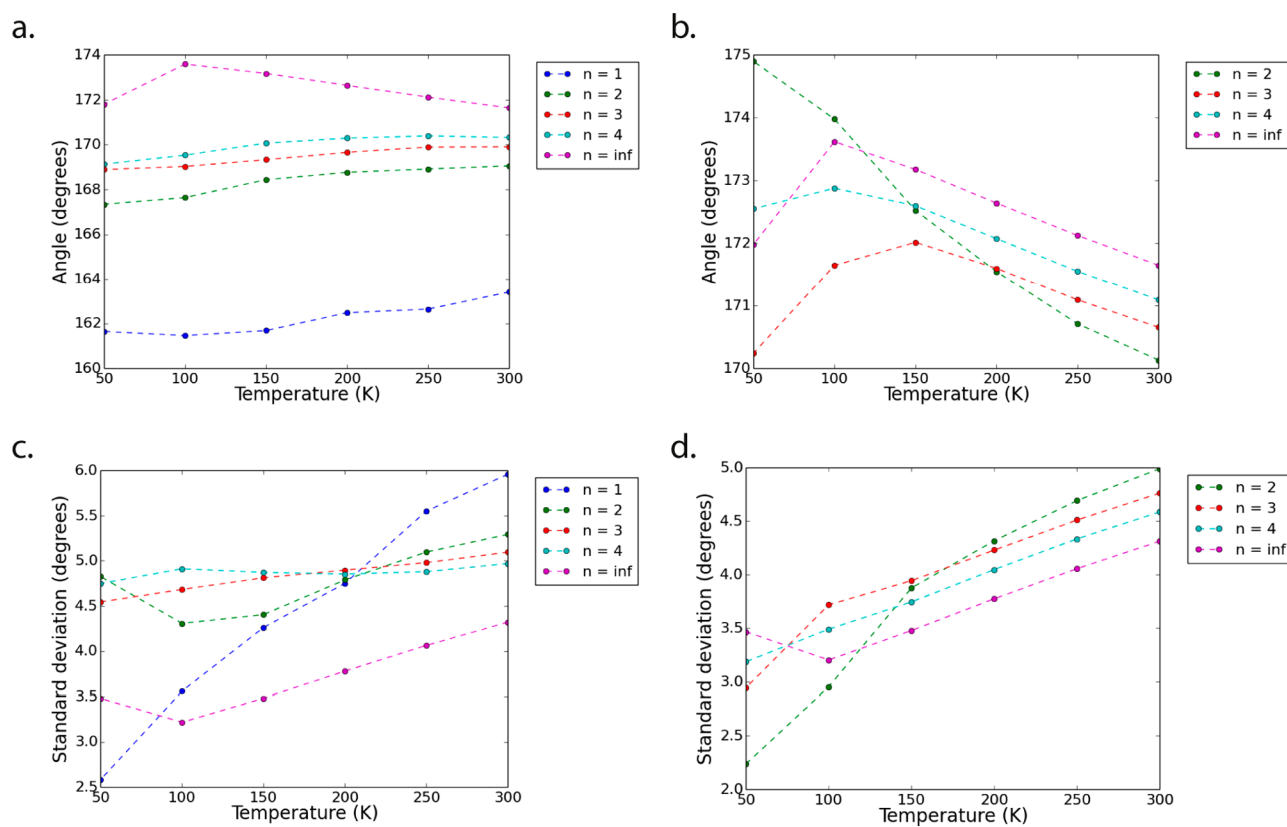


**Figure 2.** Pb–I–Pb angles in the different simulated structures. (a) Average Pb–I–Pb angles in the lead–iodide layer. (b) Average Pb–I–Pb angles perpendicular to the lead–iodide layer. (c) Standard deviation of the Pb–I–Pb angles in the lead–iodide layer. (d) Standard deviation of the Pb–I–Pb angles perpendicular to the lead–iodide layer.

smaller standard deviation. This procedure is illustrated in Figures 1a–c with an example of a histogram and a fit, while in Figure 1d the average standard deviation of each structure is plotted as a function of temperature.

In Figure 1d, it can be seen that lowering the temperature leads to the expected trend of a reduced movement of the lead atoms around their equilibrium position. Furthermore, at high temperatures the general trend is that the movement of lead atoms decreases on increasing the number of lead–iodide layers. This shows that increasing the number of stacked lead–iodide layers makes the structure more rigid. At 50 K, the lowest temperature simulated, all the structures except for the  $n = 1$  material exhibit a more or less identical standard deviation of the position of the lead atoms.

While all the other structures have a similar change in standard deviation with temperature, for the  $n = 1$  the dependence on temperature is much stronger. This results in a substantial difference between the  $n = 1$  and the other structures at higher temperatures. Moreover, the gap between the standard deviations in the Pb positions between  $n = 1$  and  $n = 2$  is much larger than between all other structures. This shows that the  $n = 1$  structure is considerably less rigid than the  $n > 1$  structures at all temperatures.

To obtain a more detailed understanding of the effects of temperature on the structure of the inorganic framework of the different RP compounds, we have examined the average Pb–I–Pb angles as a function of the temperature (Figure 2). The Pb–I–Pb angle corresponds to the mutual angle between two neighboring octahedra and will therefore give an indication of the tilting of the octahedra in each structure. In a perfectly cubic structure, the Pb–I–Pb angle will be  $180^\circ$ , but any tilting will result in a smaller angle, and the smaller the angle is the more tilted the octahedra are. Furthermore, because of thermal motion, a cubic structure will show a slightly lower average Pb–I–Pb angle than  $180^\circ$ . We make a distinction between the Pb–I–Pb angles that are present in the lead–iodide layers (Figure 2a) and the Pb–I–Pb angles that are perpendicular to the lead–iodide layers (Figure 2b), and we also show the standard deviations for both sets of angles in Figures 2c and 2d. The Pb–I–Pb angles within the lead–iodide layer are two separate angles, but as can be seen in Figure S3 there is no difference between these two angles in the simulated structures.

The first clear trend observed from Figure 2a is that the average Pb–I–Pb angle in the layer approaches  $180^\circ$  as the number of lead–iodide layers increases. It is also clear that the tilting of the octahedra in the  $n = 1$  structure is substantially more pronounced than in their counterparts with  $n > 1$ . This can be seen from the large gap in average Pb–I–Pb angle for the  $n = 1$  as compared to all other structures. As the temperature is lowered, all the 2D structures show a similar gradual decrease in the average angle. The exception to this trend is the 3D perovskite where the average angle initially increases gradually before decreasing significantly between 100 and 50 K. The gradual increase can be due to structural changes but can also be a result of statistical effects as noted above. The initially decreasing temperature leads to a reduction in the thermal motion of the resulting in an average angle closer to the optimal Pb–I–Pb angle of the structure, which is close to  $180^\circ$ . The sudden decrease in the average angle between 100 and 50 K cannot, however, be explained by such statistical effects and must therefore be due to distinct structural changes in the materials, a phase transition. This is

well-known for 3D perovskites but happens at higher temperatures than observed in these simulations.<sup>43</sup>

The Pb–I–Pb angle perpendicular to the lead–iodide layer for the 3D perovskite (Figure 2b) shows exactly the same behavior as in the lead–iodide layer. This is not surprising since the 3D perovskite is not a layered structure, and all three principal directions are roughly equivalent. For the 2D structures, however, significant differences arise between the perpendicular and the in-layer angles. First, all compounds show a larger Pb–I–Pb angle in the direction perpendicular to the lead–iodide layer than in the layer at all temperatures. Second, decreasing the temperature has a very different effect. The  $n = 3$  and  $n = 4$  now behave more like the 3D structure, where at first the angle increases and then at a specific temperature it decreases. For the  $n = 4$  the decrease happens between 100 and 50 K and is very small. Therefore, it is difficult to say whether this is due to a phase transition in the material or a slight alteration in optimal angles. In the case of the  $n = 3$  the decrease in the angle is more profound, starting with a slight decrease between 150 and 100 K followed by a steeper decrease between 100 and 50 K. This is very similar to the behavior of the 3D perovskite and suggests that the  $n = 3$  goes through a phase transition at similar temperatures as the 3D perovskite. The  $n = 2$  structure exhibits a very different behavior. In this case, the Pb–I–Pb angle increases steadily with decreasing temperature, indicating less tilting of the octahedra.

The  $n = 1$  structure has no Pb–I–Pb angle perpendicular to the lead–iodide layer. To show some comparison of the out-of-layer tilting of that structure versus the other structures, we define an angle between the lead–iodide plane and the out-of-layer iodides (see Figure S2). This analysis shows that the  $n = 1$  has the largest tilting in the out-of-layer direction by some margin as it does in the in-layer direction (Figure 2a); i.e., the structure is more flexible overall.

From Figures 2c and 2d it can be seen that the standard deviation of the angles decreases in most cases with the temperature, as we would expect from the decreased motion of the atoms. There are, however, some notable exceptions. For instance, the standard deviation for the 3D perovskite becomes slightly larger when the material goes through its phase transition. This can be explained by the definition of the angle adopted here. Because the Pb–I–Pb angle is defined in the range from  $0$ – $180^\circ$ , the distribution of angles is one-sided when the optimal angle is close to  $180^\circ$ . If the optimal angle shifts to a slightly lower angle, the distribution will become two-sided and therefore a bit broader.

**Rotational Dynamics of the Methylammonium.** The structure and dynamics of the inorganic Pb–I lattices are intricately linked to the presence and dynamics of the organic cations. Therefore, we now turn to the MA ions and their dynamics in the different structures. To compare the rotational dynamics of the MA ions, we evaluate the rotational autocorrelation function (ACF) of the MA ions averaged over the number of MA ions ( $N_{\text{ion}}$ ) and over all possible initial times  $t_0$  during the simulation time ( $N_{t_0}$ ).

$$A(t) = \langle \hat{n}(t) \cdot \hat{n}(0) \rangle = \frac{1}{N_{\text{ion}}} \sum_i \frac{1}{N_{t_0}} \sum_{t_1=t+t_0} \hat{n}_i(t_1) \cdot \hat{n}_i(t_0)$$

The ACF gives an indication of whether the MA ions can rotate freely and on the time scale at which they reorient. If the MA ions are fully free to rotate and can obtain any orientation,

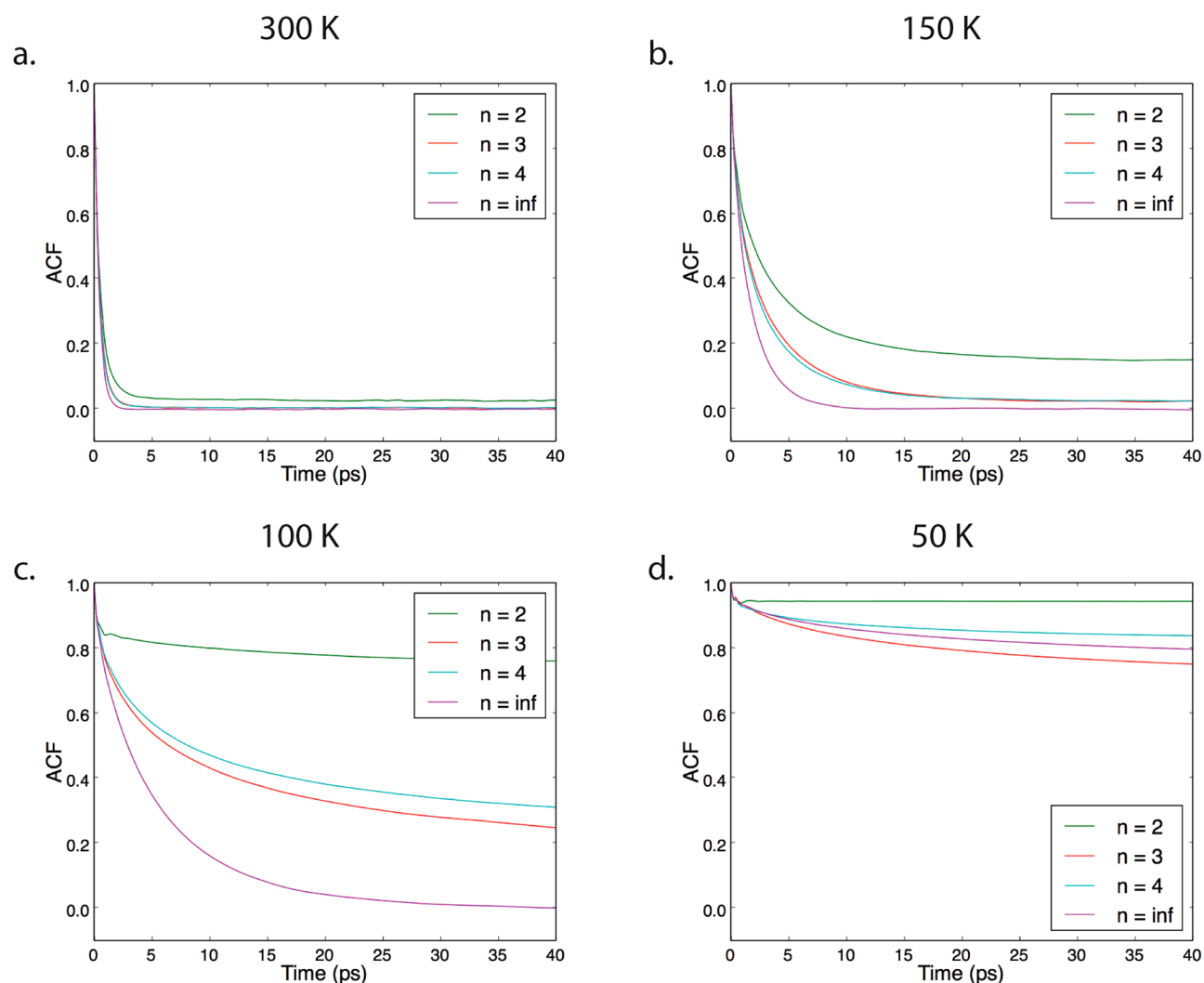


**Figure 3.** Rotational autocorrelation function for MA ions in the different structures at (a) 300, (b) 150, (c) 100, and (d) 50 K.

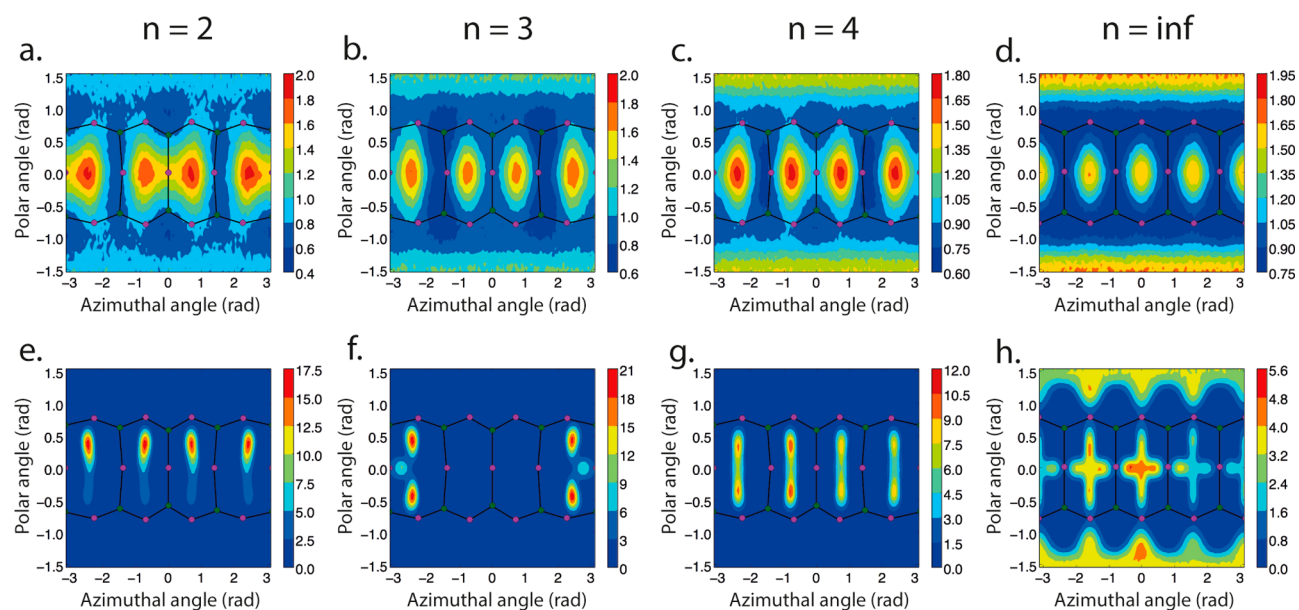


**Figure 4.** Normalized heat maps of MA ion directions in the structures examined at 300 K (top row) and 50 K (bottom row): (a)  $n = 2$  at 300 K, (b)  $n = 3$  at 300 K, (c)  $n = 4$  at 300 K, (d)  $n = \infty$  at 300 K, (e)  $n = 2$  at 50 K, (f)  $n = 3$  at 50 K, (g)  $n = 4$  at 50 K, and (h)  $n = \infty$  at 50 K.

the ACF value will decay to zero, indicating a random distribution of directions, on average. The time scale on which this happens is the rotational diffusion time. However, if the rotational motion is restricted, for instance by directional interactions with the Pb–I lattice, the ACF will not fully decay to zero but saturate at a certain value. This saturation value indicates how much freedom the MA ion has to move around. In Figure 3 the ACF of the MA ions in the structure that include MA ions is shown at the following temperatures: (a) 300, (b) 150, (c) 100, and (d) 50 K. The reason we focus more on the lower temperatures is that at high temperature there is no significant change in behavior with temperature.

As can be seen from Figure 3a, the ACF reaches a plateau within the first 5 ps for all structures at 300 K. The most interesting observation is that for the  $n = 2$  structure the ACF does not fully decay to zero. This means that at this temperature the rotation of the MA ions in the  $n = 2$  material is not completely free, and some forbidden orientations exist. The data in Figure 3 also show that for all temperatures the  $n = 2$  structure always has the highest ACF value, by some margin. This indicates that the MA ions in this structure have the least freedom to rotate as compared to the other compounds. This is interesting since in the  $n = 2$  structure the environment in which the MA ions rotate differs considerably from the other structures. In this material, each MA layer is flanked by two BA layers on each side, while the MA layers in the structures with  $n > 2$  have at least one layer of MA as a neighbor, at least on one side. This indicates that the neighboring MA layers increase each other's ability to move freely around.

At 150 K, shown in Figure 3b, we see that for the  $n = \infty$  structure the ACF decays to zero within roughly 10 ps, while for  $n = 3$  and  $n = 4$  the decay is slower and saturates at a value above zero, indicating some preferential orientations. Interestingly, the plateau value of the ACF is almost identical at this temperature for  $n = 3$  and  $n = 4$ . If the temperature is lowered even more, to 100 K, we see that  $n = \infty$  still decays fastest and reaches zero in roughly 40 ps. In addition, at this temperature the ACF of the  $n = 3$  decays faster than the ACF for the  $n = 4$  structure, although the difference is small. This is the same temperature as we earlier saw changes in the octahedral tilting of the lead–iodide lattice for the  $n = 3$  structure.

When considering the results at 50 K in Figure 4d, we see that the ACF of  $n = 3$  still decays to a lower value than for  $n = 4$  and is now also lower than the one for  $n = \infty$ . The  $n = \infty$  structure has a significantly higher ACF plateau value at this temperature, and the MA ions seem now much more static than before. This occurs at the same temperature where we previously saw the average Pb–I–Pb angle change and is consistent with a phase transition occurring in the material.<sup>38,40</sup> The structural changes of both  $n = 3$  and  $\infty$  seem to affect the motion of their MA ions but in an opposite fashion. In the case of the  $n = 3$  the ACF value decays faster compared to the  $n = 4$  structure, meaning more movement of the MA ions, while for  $n = \infty$  the ACF gets higher and saturates at higher value than the  $n = 3$  structure, indicating significantly less movement. This shows that the relation between structural changes and MA movement is not straightforward and influenced by multiple factors. These factors include the thickness of the lead–iodide layers that affect their rigidity and the interaction with ions in neighboring layers (either BA or MA).

To analyze the dynamics and behavior of the MA ions in the different structures in more detail, we plot in Figure 4 normalized heat maps indicating the occurrence of different

directions of the MA ions in terms of the polar and azimuthal angles, throughout a simulation at 300 and 50 K. On the heat maps we have also plotted the relative positions of iodides and leads with respect to the MA ions based on the initial structure of the system. The normalization is done to compensate for the fact that we are plotting spherical surface on rectangular grid and results in all values larger than one to represent a higher density of MA ions than random distribution would predict and values lower than one representing less density than if the ions were distributed randomly.

If we first focus on the 300 K simulation for  $n = \infty$ , we see six high-density areas indicating preferential orientations of the MA ions. These areas correspond to structures where the CN axis of MA points to centers of the facets of the tetragonal lead–iodide surroundings. The reason that these orientations are preferred over others is the possibility of forming hydrogen bonding between the hydrogens on the MA nitrogen atoms and the iodides in the Pb–I layers. At high temperatures these hydrogen bonds are short-lived, and after they break up, the MA ion can jump to the next iodide forming a new hydrogen bond. These jumps happen rapidly and seem to happen primarily within a lead–iodide facet, resulting in a high density of MA ions pointing toward each facet.

For  $n = \infty$  the six tetragonal facets are roughly equivalent as the organic cation on the other side of the facet is always another MA ion. This is not the case for the 2D structures where the top and bottom facets have either in all or most cases at least one BA ion as a neighbor. These structures also show different behavior than the  $n = \infty$  material at high temperatures, where top and bottom facets are less occupied than the others. This becomes increasingly visible when the number of layers is decreased (note the difference in the color scale for different materials). The  $n = 2$  structure has even fewer MA ions pointing to the top and bottom facets than random orientation predicts. This is caused by the repulsion with the BA ions that are in a fixed global orientation with respect to the Pb–I layers. As a result, the MA ions are prevented from taking a certain orientation and explains why the ACF for  $n = 2$  does not reach a plateau at zero.

If we now focus on the 50 K heat maps, we see that the  $n = \infty$  structure has a similar MA ion distribution as at 300 K in the sense that still all the orientations are available for the MA ions. What is different in this case is that we clearly see higher density of MA ions next to the iodides where the hydrogen bonds are formed. This happens since at low temperature the thermal motion of the MA ions is reduced and the hydrogen bonds live longer. Therefore, the MA will spend more time at the most preferred position, next to the iodide.

For all the other structures the difference between the high and low temperature is clearer. In all the cases the top and bottom facets are more or less unoccupied at 50 K, meaning that almost no MA ions point in this direction at low temperatures. The high-density areas next to the iodides are also clearer than for the  $n = \infty$ , and for the occupied facets not all positions next to iodide have high density. For the  $n = 2$  only the position next to the top iodide is highly occupied with some minor occupation next to the lower iodides, meaning that the MA ions are really fixed in a certain orientation and rarely move to another orientation. This is consistent with the decay of the ACF for  $n = 2$  structure at 50 K, which showed very little decay (see above). For the  $n = 4$  structure the preferred orientations are very similar to the  $n = 2$  material. The main difference is that the alignment next to the bottom

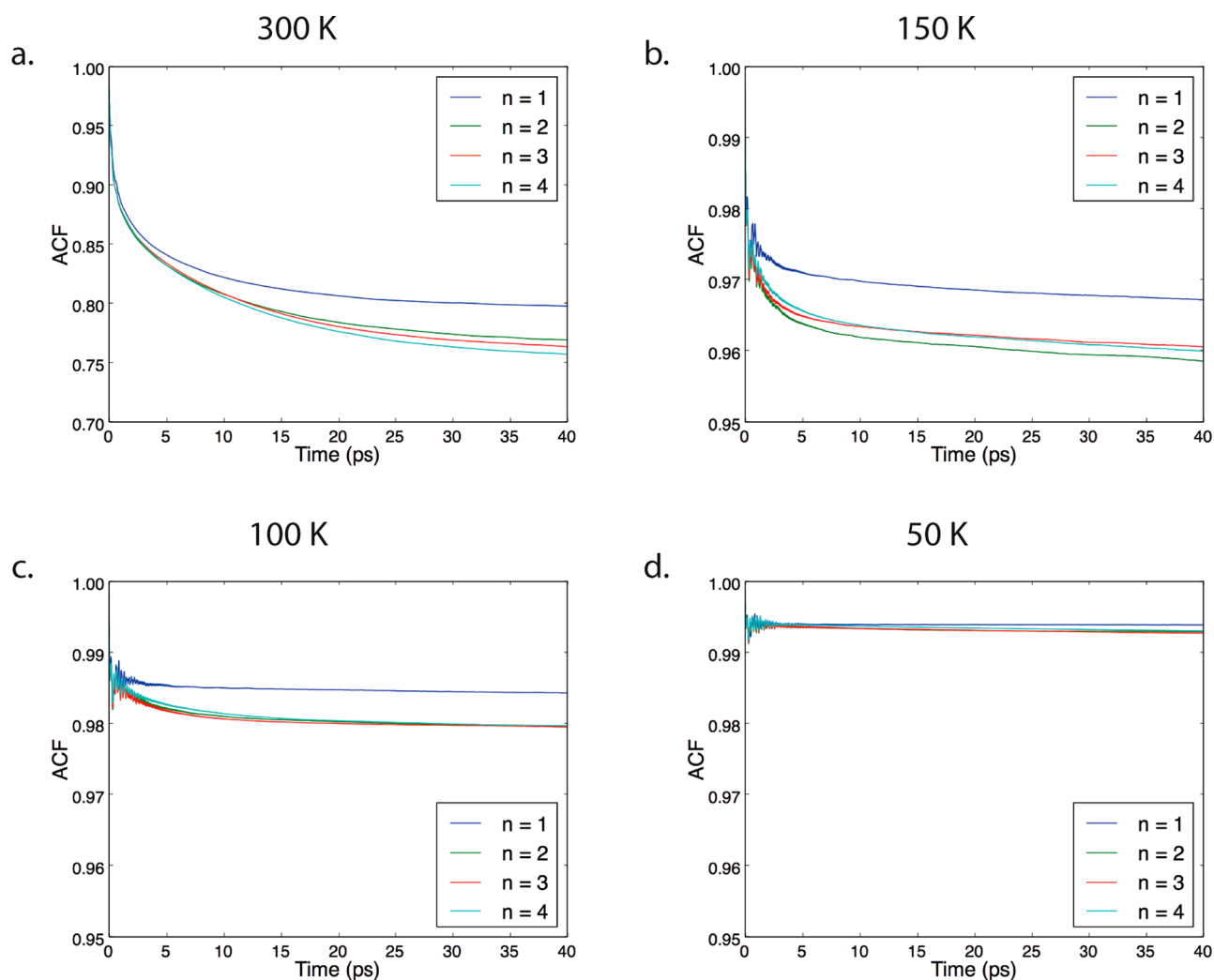


**Figure 5.** Rotational autocorrelation function for N–C bond in BA ions in the different structures at (a) 300, (b) 150, (c) 100, and (d) 50 K.

iodide is now roughly equally probable as the alignment next to the top iodide. We also see that between these preferable areas there is a path with some occupancy; this implies that over the course of the simulation all or some of the MA ions manage to jump between these positions. This explains why the ACF of the  $n = 4$  compound reaches a plateau at a significantly lower value than for  $n = 2$ .

Once again, the  $n = 3$  structure shows a somewhat different behavior compared to the others. For some reason the  $n = 3$  structure only has MA occupancy in two tetragonal facets. We attribute this to the observed structural changes in the Pb–I lattice, accompanied by octahedral tilting at low temperatures, as seen in the change in the average Pb–I–Pb angles in Figure 2b. As the octahedra tilt, certain orientations of the MA ion become preferable because of steric effects. As was the case for  $n = 4$  the areas next to the top and bottom iodide are the preferred areas, and there is a path with some occupancy between the two. The difference is that now there is an area on the path next to one of the middle iodides, which also has an appreciable occupancy. This means that when the MA ion is jumping between favorable positions next to the top and bottom iodide it can occupy an intermediate orientation in the case of  $n = 3$ . This decreases the energy barrier needed to make the jump and therefore allowing the MA ion to move more

rapidly between the preferred areas. This explains why the  $n = 3$  structure has the lowest ACF plateau at 50 K.

**Rotational Dynamics of the Butylammonium.** Finally, we consider whether there is any difference in the behavior of the BA ions for the different structures. To do this, we compare the ACF of the N–C bond in BA for the different structures at some of the simulated temperatures in Figure 5. It is important to keep in mind that these ACF plots will differ from the ones for the MA ions. The MA ion is a small ion that can rotate relatively freely as long as nothing hampers its motion. The BA ion, on the other hand, is bulkier and is only surrounded by Pb–I on one side. Therefore, it cannot reorient completely and ACF will not reach zero at any temperature.

Upon comparison of the ACF for BA in the different structures, the main observation is that the  $n = 1$  structure plateaus at significantly higher ACF value than the other structures and thus reorients less. This surprising observation is related to the lack of MA ions in the structure. The BA ion interacts strongly with the Pb–I lattice for the  $n = 1$  structure. When the inorganic layer becomes thicker and MA ions are introduced, this leads to a screening effect with a net repulsive interaction between the MA and BA ions. The overall result of this is an increased rotational freedom for structures with  $n > 1$ .

## CONCLUSIONS

In this paper we have analyzed the structural dynamics of Ruddlesden–Popper perovskites using model potential molecular dynamics simulations. Calculations were performed for different thicknesses of the inorganic layer. The results show that the dimensionality (layer thickness) of 2D Ruddlesden–Popper perovskites has a clear, but not always a straightforward, effect on the structure and dynamics of both the inorganic and organic part of the perovskite. In the case of the inorganic part, we see that the rigidity increases as the number of inorganic layers is increased and that the  $n = 1$  structure is substantially less rigid than the structures with  $n > 1$ . In addition, we clearly observe phase transition where the tilting of the average Pb–I–Pb angles changes for the  $n = 3$  and  $n = \infty$  structures, but in the other structures this is not as clearly visible.

In the organic part, certain orientations of MA ions are not as favorable in the case of the 2D perovskite when compared to its 3D counterpart. This clearly shows the effect of the edges of the perovskite structure where relatively static BA cations are present. This nonuniform surrounding leads to restricted rotational freedom of the MA cations in the 2D structures, as compared to the 3D material. The motion of the organic cations is also directly linked to deformations in the inorganic lattice, and clear differences are observed for different thicknesses of the inorganic layer. The results highlight the interplay between the inorganic and organic part in these materials, which is complex and not necessarily uniform for all the different structures. An improved understanding of the structural dynamics is essential for systematically engineering the electronic properties of Ruddlesden–Popper perovskites as the electronic structure is directly linked to the structure of the inorganic lattice and the rotational dynamics of the dipolar organic cations.

## ASSOCIATED CONTENT

### Supporting Information

The Supporting Information is available free of charge at <https://pubs.acs.org/doi/10.1021/acs.jpcc.0c05225>.

All the parameters used for the molecular dynamics force field (Tables S1–S6); comparison of rotational autocorrelation of 3D methylammonium lead iodide simulated with force field with and without full formal charges (Figure S1); description of the out-of-layer iodide angle along with graphs (Figure S2); the difference between the two in layer Pb–I–Pb angles (Figure S3) (PDF)

## AUTHOR INFORMATION

### Corresponding Author

Ferdinand C. Grozema – Department of Chemical Engineering, Faculty of Applied Sciences, Delft University of Technology, 2629 HZ Delft, The Netherlands; [orcid.org/0000-0002-4375-799X](https://orcid.org/0000-0002-4375-799X); Email: [f.c.grozema@tudelft.nl](mailto:f.c.grozema@tudelft.nl)

### Authors

Magnus B. Fridriksson – Department of Chemical Engineering, Faculty of Applied Sciences, Delft University of Technology, 2629 HZ Delft, The Netherlands

Sudeep Maheshwari – Department of Chemical Engineering, Faculty of Applied Sciences, Delft University of Technology, 2629 HZ Delft, The Netherlands

Complete contact information is available at: <https://pubs.acs.org/10.1021/acs.jpcc.0c05225>

## Notes

The authors declare no competing financial interest.

## ACKNOWLEDGMENTS

The research leading to these results in the Delft University of Technology has received funding from the European Research Council Horizon 2020 ERC Grant Agreement No. 648433.

## REFERENCES

- (1) Kojima, A.; Teshima, K.; Shirai, Y.; Miyasaka, T. Organometal Halide Perovskites as Visible-Light Sensitizers for Photovoltaic Cells. *J. Am. Chem. Soc.* **2009**, *131* (17), 6050–6051.
- (2) Lee, M. M.; Teuscher, J.; Miyasaka, T.; Murakami, T. N.; Snaith, H. J. Efficient Hybrid Solar Cells Based on Meso-Structured Organometal Halide Perovskites. *Science* **2012**, *338* (6107), 643–647.
- (3) Snaith, H. J. Present Status and Future Prospects of Perovskite Photovoltaics. *Nat. Mater.* **2018**, *17* (5), 372–376.
- (4) National Renewable Energy Laboratory (NREL) Best Research-Cell Efficiencies Chart. <https://www.nrel.gov/pv/cell-efficiency.html> (accessed 2020-06).
- (5) Tan, Z.-K.; Moghaddam, R. S.; Lai, M. L.; Docampo, P.; Higler, R.; Deschler, F.; Price, M.; Sadhanala, A.; Pazos, L. M.; Credgington, D.; et al. Bright Light-Emitting Diodes based on Organometal Halide Perovskite. *Nat. Nanotechnol.* **2014**, *9* (9), 687–692.
- (6) Veldhuis, S. A.; Boix, P. P.; Yantara, N.; Li, M.; Sum, T. C.; Mathews, N.; Mhaisalkar, S. G. Perovskite Materials for Light-Emitting Diodes and Lasers. *Adv. Mater.* **2016**, *28* (32), 6804–34.
- (7) Xu, W.; Hu, Q.; Bai, S.; Bao, C.; Miao, Y.; Yuan, Z.; Borzda, T.; Barker, A. J.; Tyukalova, E.; Hu, Z.; et al. Rational Molecular Passivation for High-Performance Perovskite Light-Emitting Diodes. *Nat. Photonics* **2019**, *13* (6), 418–424.
- (8) Dou, L.; Yang, Y.; You, J.; Hong, Z.; Chang, W.-H.; Li, G.; Yang, Y. Solution-Processed Hybrid Perovskite Photodetectors with High Detectivity. *Nat. Commun.* **2014**, *5* (1), 5404.
- (9) Leung, S. F.; Ho, K. T.; Kung, P. K.; Hsiao, V. K. S.; Alshareef, H. N.; Wang, Z. L.; He, J. H. A Self-Powered and Flexible Organometallic Halide Perovskite Photodetector with Very High Detectivity. *Adv. Mater.* **2018**, *30* (8), 1704611.
- (10) Chen, S.; Roh, K.; Lee, J.; Chong, W. K.; Lu, Y.; Mathews, N.; Sum, T. C.; Nurmikko, A. A Photonic Crystal Laser from Solution Based Organo-Lead Iodide Perovskite Thin Films. *ACS Nano* **2016**, *10* (4), 3959–67.
- (11) Stoumpos, C. C.; Malliakas, C. D.; Peters, J. A.; Liu, Z.; Sebastian, M.; Im, J.; Chasapis, T. C.; Wibowo, A. C.; Chung, D. Y.; Freeman, A. J.; et al. Crystal Growth of the Perovskite Semiconductor CsPbBr<sub>3</sub>: A New Material for High-Energy Radiation Detection. *Cryst. Growth Des.* **2013**, *13* (7), 2722–2727.
- (12) Wei, H.; Fang, Y.; Mulligan, P.; Chirazzini, W.; Fang, H.-H.; Wang, C.; Ecker, B. R.; Gao, Y.; Loi, M. A.; Cao, L.; et al. Sensitive X-Ray Detectors made of Methylammonium Lead Tribromide Perovskite Single Crystals. *Nat. Photonics* **2016**, *10* (5), 333–339.
- (13) Wei, H.; Huang, J. Halide Lead Perovskites for Ionizing Radiation Detection. *Nat. Commun.* **2019**, *10* (1), 1066.
- (14) Berhe, T. A.; Su, W.-N.; Chen, C.-H.; Pan, C.-J.; Cheng, J.-H.; Chen, H.-M.; Tsai, M.-C.; Chen, L.-Y.; Dubale, A. A.; Hwang, B.-J. Organometal Halide Perovskite Solar Cells: Degradation and Stability. *Energy Environ. Sci.* **2016**, *9* (2), 323–356.
- (15) Niu, G.; Guo, X.; Wang, L. Review of Recent Progress in Chemical Stability of Perovskite Solar Cells. *J. Mater. Chem. A* **2015**, *3* (17), 8970–8980.
- (16) Mitzi, D. B. Synthesis, Crystal Structure, and Optical and Thermal Properties of (C<sub>4</sub>H<sub>9</sub>NH<sub>3</sub>)<sub>2</sub>MI<sub>4</sub> (M = Ge, Sn, Pb). *Chem. Mater.* **1996**, *8* (3), 791–800.
- (17) Smith, I. C.; Hoke, E. T.; Solis-Ibarra, D.; McGehee, M. D.; Karunadasa, H. I. A Layered Hybrid Perovskite Solar-Cell Absorber

with Enhanced Moisture Stability. *Angew. Chem., Int. Ed.* **2014**, *53* (42), 11232–5.

(18) Cao, D. H.; Stoumpos, C. C.; Farha, O. K.; Hupp, J. T.; Kanatzidis, M. G. 2D Homologous Perovskites as Light-Absorbing Materials for Solar Cell Applications. *J. Am. Chem. Soc.* **2015**, *137* (24), 7843–50.

(19) Dou, L.; Wong, A. B.; Yu, Y.; Lai, M.; Kornienko, N.; Eaton, S. W.; Fu, A.; Bischak, C. G.; Ma, J.; Ding, T.; et al. Atomically Thin Two-Dimensional Organic-Inorganic Hybrid Perovskites. *Science* **2015**, *349* (6255), 1518–21.

(20) Liu, J.; Xue, Y.; Wang, Z.; Xu, Z.-Q.; Zheng, C.; Weber, B.; Song, J.; Wang, Y.; Lu, Y.; Zhang, Y.; et al. Two-Dimensional CH<sub>3</sub>NH<sub>3</sub>PbI<sub>3</sub> Perovskite: Synthesis and Optoelectronic Application. *ACS Nano* **2016**, *10* (3), 3536–3542.

(21) Stoumpos, C. C.; Cao, D. H.; Clark, D. J.; Young, J.; Rondinelli, J. M.; Jang, J. I.; Hupp, J. T.; Kanatzidis, M. G. Ruddlesden–Popper Hybrid Lead Iodide Perovskite 2D Homologous Semiconductors. *Chem. Mater.* **2016**, *28* (8), 2852–2867.

(22) Liao, Y.; Liu, H.; Zhou, W.; Yang, D.; Shang, Y.; Shi, Z.; Li, B.; Jiang, X.; Zhang, L.; Quan, L. N.; et al. Highly Oriented Low-Dimensional Tin Halide Perovskites with Enhanced Stability and Photovoltaic Performance. *J. Am. Chem. Soc.* **2017**, *139* (19), 6693–6699.

(23) Spanopoulos, I.; Hadar, I.; Ke, W.; Tu, Q.; Chen, M.; Tsai, H.; He, Y.; Shekhawat, G.; Dravid, V. P.; Wasielewski, M. R.; et al. Uniaxial Expansion of the 2D Ruddlesden–Popper Perovskite Family for Improved Environmental Stability. *J. Am. Chem. Soc.* **2019**, *141* (13), 5518–5534.

(24) Quan, L. N.; Yuan, M.; Comin, R.; Voznyy, O.; Beaugard, E. M.; Hoogland, S.; Buin, A.; Kirmani, A. R.; Zhao, K.; Amassian, A.; et al. Ligand-Stabilized Reduced-Dimensionality Perovskites. *J. Am. Chem. Soc.* **2016**, *138* (8), 2649–55.

(25) Yuan, M.; Quan, L. N.; Comin, R.; Walters, G.; Sabatini, R.; Voznyy, O.; Hoogland, S.; Zhao, Y.; Beaugard, E. M.; Kanjanaboos, P.; et al. Perovskite Energy Funnels for Efficient Light-Emitting Diodes. *Nat. Nanotechnol.* **2016**, *11* (10), 872–877.

(26) Gao, Y.; Shi, E.; Deng, S.; Shiring, S. B.; Snider, J. M.; Liang, C.; Yuan, B.; Song, R.; Janke, S. M.; Liebman-Peláez, A.; et al. Molecular Engineering of Organic–Inorganic Hybrid Perovskites Quantum Wells. *Nat. Chem.* **2019**, *11* (12), 1151–1157.

(27) Passarelli, J. V.; Fairfield, D. J.; Sather, N. A.; Hendricks, M. P.; Sai, H.; Stern, C. L.; Stupp, S. I. Enhanced Out-of-Plane Conductivity and Photovoltaic Performance in *n* = 1 Layered Perovskites through Organic Cation Design. *J. Am. Chem. Soc.* **2018**, *140* (23), 7313–7323.

(28) Du, K. -z.; Tu, Q.; Zhang, X.; Han, Q.; Liu, J.; Zauscher, S.; Mitzi, D. B. Two-Dimensional Lead(II) Halide-Based Hybrid Perovskites Templated by Acene Alkylamines: Crystal Structures, Optical Properties, and Piezoelectricity. *Inorg. Chem.* **2017**, *56* (15), 9291–9302.

(29) Gelvez-Rueda, M. C.; Fridriksson, M. B.; Dubey, R. K.; Jager, W. F.; van der Stam, W.; Grozema, F. C. Overcoming the Exciton Binding Energy in Two-Dimensional Perovskite Nanoplatelets by Attachment of Conjugated Organic Chromophores. *Nat. Commun.* **2020**, *11* (1), 1901.

(30) Maheshwari, S.; Savenije, T. J.; Renaud, N.; Grozema, F. C. Computational Design of Two-Dimensional Perovskites with Functional Organic Cations. *J. Phys. Chem. C* **2018**, *122* (30), 17118–17122.

(31) Zibouche, N.; Islam, M. S. Structure-Electronic Property Relationships of 2D Ruddlesden–Popper Tin- and Lead-based Iodide Perovskites. *ACS Appl. Mater. Interfaces* **2020**, *12* (13), 15328–15337.

(32) Seitz, M.; Magdaleno, A. J.; Alcazar-Cano, N.; Melendez, M.; Lubbers, T. J.; Walraven, S. W.; Pakdel, S.; Prada, E.; Delgado-Buscalioni, R.; Prins, F. Exciton Diffusion in Two-Dimensional Metal-Halide Perovskites. *Nat. Commun.* **2020**, *11* (1), 2035.

(33) Deng, S.; Shi, E.; Yuan, L.; Jin, L.; Dou, L.; Huang, L. Long-Range Exciton Transport and Slow Annihilation in Two-Dimensional Hybrid Perovskites. *Nat. Commun.* **2020**, *11* (1), 664.

(34) Maheshwari, S.; Patwardhan, S.; Schatz, G. C.; Renaud, N.; Grozema, F. C. The Effect of the Magnitude and Direction of the Dipoles of Organic Cations on the Electronic Structure of Hybrid Halide Perovskites. *Phys. Chem. Chem. Phys.* **2019**, *21* (30), 16564–16572.

(35) Gallop, N. P.; Selig, O.; Giubertoni, G.; Bakker, H. J.; Rezus, Y. L. A.; Frost, J. M.; Jansen, T. L. C.; Lovrincic, R.; Bakulin, A. A. Rotational Cation Dynamics in Metal Halide Perovskites: Effect on Phonons and Material Properties. *J. Phys. Chem. Lett.* **2018**, *9* (20), 5987–5997.

(36) Mao, L.; Stoumpos, C. C.; Kanatzidis, M. G. Two-Dimensional Hybrid Halide Perovskites: Principles and Promises. *J. Am. Chem. Soc.* **2019**, *141* (3), 1171–1190.

(37) Plimpton, S. Fast Parallel Algorithms for Short-Range Molecular Dynamics. *J. Comput. Phys.* **1995**, *117* (1), 1–19.

(38) Mattoni, A.; Filippetti, A.; Saba, M. I.; Delugas, P. Methylammonium Rotational Dynamics in Lead Halide Perovskite by Classical Molecular Dynamics: The Role of Temperature. *J. Phys. Chem. C* **2015**, *119* (30), 17421–17428.

(39) Ponder, J. W.; Case, D. A. Force Fields for Protein Simulations. *Adv. Protein Chem.* **2003**, *66*, 27–85.

(40) Maheshwari, S.; Fridriksson, M. B.; Seal, S.; Meyer, J.; Grozema, F. C. The Relation between Rotational Dynamics of the Organic Cation and Phase Transitions in Hybrid Halide Perovskites. *J. Phys. Chem. C* **2019**, *123* (23), 14652–14661.

(41) Breneman, C. M.; Wiberg, K. B. Determining Atom-Centered Monopoles from Molecular Electrostatic Potentials. The Need for High Sampling Density in Formamide Conformational Analysis. *J. Comput. Chem.* **1990**, *11* (3), 361–373.

(42) Frisch, M. J.; Trucks, G. W.; Schlegel, H. B.; Scuseria, G. E.; Robb, M. A.; Cheeseman, J. R.; Scalmani, G.; Barone, V.; Petersson, G. A.; Nakatsuji, H.; et al. *Gaussian 09, Rev. A.02*; Gaussian, Inc.: Wallingford, CT, 2016.

(43) Stoumpos, C. C.; Malliakas, C. D.; Kanatzidis, M. G. Semiconducting Tin and Lead Iodide Perovskites with Organic Cations: Phase Transitions, High Mobilities, and Near-Infrared Photoluminescent Properties. *Inorg. Chem.* **2013**, *52* (15), 9019–9038.